Effect of Segregation of Secondary Phase Particles and "S" Line on Tensile Fracture Behavior of Friction Stir-Welded 2024Al-T351 Joints

Z. ZHANG, B.L. XIAO, and Z.Y. MA

A 5-mm-thick 2024Al-T351 plate was friction stir welded (FSWed) at welding speeds of 100, 200, and 400 mm min^{-1} with a constant rotation rate of 800 rpm, and the microstructure and tensile fracture behavior of the joints were investigated in detail. FSW resulted in the redistribution of secondary phase particles along the recrystallized grain boundaries at the nugget zone (NZ), forming linear segregation bands consisting of secondary phase particles. The segregation bands, mainly present in the shoulder-driven zone, were believed to result from periodic material flow, with the average band spacing on the longitudinal and horizontal cross sections equal to the tool advancement per revolution. At a low welding speed of 100 mm min^{-1}, in spite of the highest density of segregation bands, the FSWed 2024Al-T351 joint fractured along the low hardness zone (LHZ) of the heat-affected zone because of large hardness gap between NZ and LHZ. Increasing the welding speed to 200 and 400 mm min^{-1} reduced both the hardness gap between NZ and LHZ and the density of segregation bands. In this case, the segregation bands played a role, resulting in unusual fracture of the joints along the segregation bands. The "S" line originated from the oxide film on the initial butting surfaces and did not affect the fracture behavior of the FSWed 2024Al-T351 joints.

DOI: 10.1007/s11661-013-1778-8

I. INTRODUCTION

2024 aluminum alloy is widely used in aerospace industry as wing and fuselage structures because of its high specific strength and fatigue resistance.[1] However, its industrial application is restricted by the process technology especially welding technology, because it is unweldable using the conventional fusion welding techniques because of its hot cracking sensitivity. The structures are usually fastened together using rivets which not only increase the weight, but also reduce the fatigue properties.[2] Therefore, a new welding method that can join the high-strength aluminum alloy is highly preferable.

Friction stir welding (FSW), a solid-state joining technique invented by The Welding Institute (TWI) of UK in 1991,[3] has many advantages, such as the lower peak temperatures and the absence of melting process of the base material (BM), avoiding solidification and liquation cracking. Thus, FSW is a new alternative welding technology for the 2024Al alloy.[4]

According to the degree of heat input and plastic deformation (plastic strain), the FSWed joint is divided into three zones on the transverse section from the core to both the retreating side (RS) and the advancing side (AS), that is, the nugget zone (NZ), thermomechanically affected zone (TMAZ), and heat-affected zone (HAZ). The highest heat input and the most severe plastic deformation occur in the NZ, followed by a decrease in heat input and plastic deformation in the TMAZ, and finally only heat input plays a role in the HAZ.

The mechanical properties of precipitation-hardened (2xxx, 6xxx, and 7xxx) aluminum alloys were dependent on the precipitate distribution. In general, there are two kinds of precipitates in precipitation-hardened aluminum alloys: one is nanoscale precipitate—it plays the major role in strengthening and is named strengthening phase in the current study; the other one is micron-scale precipitate, which plays a secondary major role in strengthening and is named secondary phase particle in the current study.

The distribution, size, and density of the strengthening phases in precipitation-hardened aluminum alloys were significantly changed in the NZ, TMAZ, and HAZ during FSW. In general, the HAZ is the low hardness zone (LHZ) and plays an important role in determining the mechanical properties and fracture behavior of the FSWed joints.[5–7] Sato *et al.*[5] found that FSWed 6063Al-T651 joint fractured at the minimum zone of the hardness curve. Ren *et al.*[6] and Liu *et al.*[7] reported that the fracture path of FSWed 6061Al-T651 joint was consistent with the lowest hardness distribution. A number of studies showed that the FSWed joints of 7050Al-T651,[8] 7050Al-T7451,[9] 7075Al-T651,[10] and 2014Al-T651[11] also failed along the LHZ during the tensile test. However, several investigations revealed that the FSWed joints of 2017Al-T351,[12] 2024Al-T351,[13] 2024Al-T4

Z. ZHANG, Assistant Professor, and B.L. XIAO and Z.Y. MA, Professors, are with the Shenyang National Laboratory for Materials Science, Institute of Metal Research, Chinese Academy of Sciences, 72 Wenhua Road, Shenyang 110016, P.R. China. Contact email: zyma@imr.ac.cn

Manuscript submitted September 8, 2012.
Article published online May 24, 2013

(T6),[14,15] 2024Al-T8,[16] and 2024Al-O[17] unusually fractured at the NZ/TMAZ interface, rather than at the LHZ. However, no detailed explanation was presented. The unusual fracture behavior showed that, for FSWed 2024Al-T351 joint, the NZ/TMAZ interface was weaker than the LHZ during tension. Thus, the microstructures near the NZ/TMAZ interface should be particularly concerned.

FSW created several special structures at the NZ, such as onion ring structure and the "S" line. Onion ring structure, consisting of several concentric rings, was a unique feature of the NZ and has approximate spacing equal to the tool advancement per revolution.[18,19] Sutton *et al.*[4] reported that the secondary phase particles were broken up and redistributed along the onion ring bands in FSWed 2024Al-T351 joint and the FSWed joint tended to fracture along the regions with high density of secondary phase particles during mixed-mode I/II monotonic fracture experiments. Moreover, it was generally believed that the "S" line consisting of broken oxide films[20] originated from the initial butting surfaces in the absence of direct observational evidence.

Afrin *et al.*,[21] Lim *et al.*[22] and Gharacheh *et al.*[23] observed oxides on the tensile fracture surface of FSWed AZ31 magnesium alloy, indicating that the fracture behavior of the FSWed joint might be associated with the "S" line. Sato *et al.*[20] systematically examined the effect of oxides of the "S" line on the root bend properties of FSWed 1050Al joint and found that the root bend property was only affected by the "S" line with continuous oxide film. Zhou *et al.*[24] and Di *et al.*[25] reported that the root "S" line with the clear oxides reduced the fatigue properties of the FSWed joints of 5083Al-H321,[24] 2024Al-T3,[24] and 7075Al-T6.[25] Fratini *et al.*[26] reported that the water cooled FSWed 7075Al-T6 joint fractured almost along the "S" line, while the air cooled FSWed joints failed at the LHZ. But the detailed evidence was absent in their work.[26]

These studies indicated that the distribution of secondary phase particles and "S" line may affect the mechanical properties of the FSWed joints under the specific condition. However, there is no study about the correlation between the distribution of secondary phase particles, "S" line, and tensile fracture behavior of FSWed 2024Al-T351 joint.

In the current study, the distribution of secondary phase particles and "S" line on three-dimensional (3D) cross sections of the FSWed 2024Al-T351 joints was examined using a manmade oxide film and tool extraction technologies. The aim is to establish the relationship between the distribution of secondary phase particles and "S" line and the fracture behavior of the FSWed 2024Al-T351 joints under varied welding parameters.

II. EXPERIMENTAL PROCEDURE

A 6.5-mm-thick commercial Alclad 2024Al-T351 rolled plate was used in the current study as the BM. The nominal chemical compositions of the plate are listed in Table I. The plates, with a length of 400 mm and a width of 70 mm, were machined on both sides to 5.0-mm thickness to remove the Alclads, and then were butt-welded along the rolling direction with a tool tilt angle of 2.75 deg using a FSW machine (China FSW Center, Beijing, China). A tool with a concave shoulder 20 mm in diameter and a threaded cylindrical pin 8 mm in diameter and 4.8 mm in length was used.

Three welding parameters representing different levels of heat input and plastic deformation were selected by fixing the rotation rate at 800 rpm and increasing the welding speed from 100 to 400 mm min^{-1}, as shown in Table II, based on the experimental results in References 6 and 7 that the tensile strength of the FSWed joints of precipitation-hardened aluminum alloys was dependent on welding speed but independent of the rotation rate. The FSWed samples were designated by brief forms; for example, "sample H-800-100" represents the FSWed joint with high heat input and plastic deformation obtained at a rotation rate of 800 rpm and a welding speed of 100 mm min^{-1}.

In order to observe the evolution process of the secondary phase particles and "S" line during FSW, the manmade oxide film and tool extraction technologies were used in Section III–C. The manmade oxide film was produced on the butting surface of the plate by

Table I. Chemical Compositions and Mechanical Properties of 2024Al-T351 Rolled Plate

Chemical Composition								Mechanical Properties		
Cu	Mg	Mn	Fe	Si	Zn	Ti	Al	YS (MPa)	UTS (MPa)	El (Pct)
3.8 to 4.9	1.2 to 1.8	0.3 to 0.9	0.50	0.50	0.25	0.15	bal	338	480	21

Table II. Welding Parameters of FSWed 2024Al-T351 Joints

Heat Input and Plastic Deformation	Rotation Rate		Welding Speed		Designation
	R (rpm)	ω (rad s^{-1})	V (mm min^{-1})	v (mm s^{-1})	
High	800	26.67π	100	1.67	H-800-100
Middle	800	26.67π	200	3.33	M-800-200
Low	800	26.67π	400	6.67	L-800-400

sectioning the plate along the rolling direction using an electric discharge machine. For the tool extraction technology, the welding tool was immediately extracted from the workpieces after welding at a pull speed of 500 mm min^{-1}. In this way, the "original" evolution process of the secondary phase particles and "S" line during FSW could be obtained.

All the samples were 3D cross sectioned to analyze the distribution of secondary phase particles and "S" line. Figure 1 shows a schematic of the three typical cross sections, that is, the transverse cross section, the longitudinal cross section, and the horizontal cross section, in which X is the welding direction, Y is the transverse direction, and Z is the plate normal direction. It should be noted that the X-O-Y and X-O-Z planes coincide with the top surface and the butting surfaces, respectively.

The microstructures of the FSWed samples were examined by scanning electron microscopy (SEM, Quanta-600, FEI Company, Hillsboro, USA) and optical microscopy (OM, Axiovert 200 MAT, Carl Zeiss. Inc., Oberkochen, Germany). To identify the secondary phase particles by SEM, polished samples were used (Section III–A). To observe the distribution of the secondary phase particles, the samples were etched using 2 pct NaOH aqueous solution and then washed with 20 pct nitric acid alcohol solution (Sections III–B and III–C). The samples for observing the grain structure were etched using Keller's reagent (2 mL water, 3 mL nitric acid, 2 mL hydrochloric acid, and 5 mL hydrofluoric acid; Section III–C).

The hardness measurement was conducted along the mid-thickness of the transverse cross section of the welds using an automatic tester (LM-247AT, LECO Corporation, St. Joseph, MI, USA) under a load of 500 g for 13 seconds. Tensile specimens were machined from the FSWed joint along the transverse direction. In order to obtain the real fracture locations of the joints, the surfaces for the tensile specimens were planned with abrasive papers to insure the equal cross-sectional area at various locations of the joints. Room-temperature tensile tests (three tensile specimens for each sample) were carried out using the Zwick-Roell testing machine at a strain rate of 4.0×10^{-4} s^{-1}. The fracture surfaces of the failed specimens were examined by SEM. The FSWed samples for the hardness and tension tests were naturally aged at room temperature for 7 days.

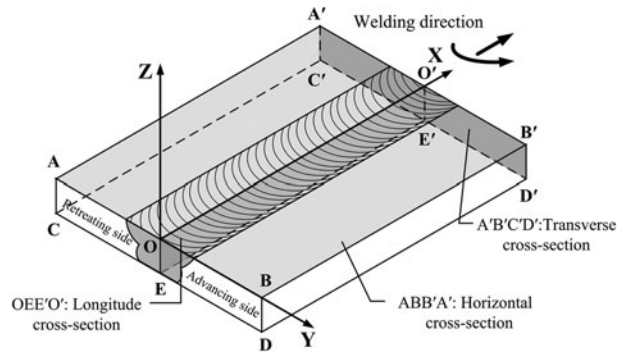

Fig. 1—A schematic of a FSW, showing the orientation of the transverse cross section, the horizontal cross section, and the longitudinal cross section relative to the tool traveling and rotating directions.

III. RESULTS

A. *Microstructures of NZ*

According to the role of shoulder and pin in the formation of the NZ, the NZ can be subdivided into three sub-zones; that is, the shoulder-driven zone (SDZ), the pin-driven zone (PDZ) and the swirl zone (SWZ).[27–29] Figure 2 shows the schematic of SDZ, PDZ, and SWZ in the FSWed 2024Al-T351 joint.

Figure 3 shows the backscattered SEM images of the BM, SDZ, PDZ, and SWZ on the transverse cross section of polished sample M-800-200. In the BM, two kinds of secondary phase particles were distributed randomly in the α-Al matrix (Figure 3(a)). The large sharp edged phases (phase I) and small smooth edged phases (phase II) were identified as Al-Cu-Mn-Fe-Si and Al_2CuMg (S-phase) phases, respectively, by the EDS analyses (Table III). This result was in agreement with that in References 30 and 31.

The microstructures of the SDZ, PDZ, and SWZ were significantly different from each other. In the SDZ, a continuous linear microstructure was observed (Figure 3(b)). Moreover, almost all the secondary phase particles in the matrix were dissolved. The magnified micrograph of the arrow zone in Figure 3(b) showed that secondary phase particles segregated at the grain boundaries and the linear microstructure consisted of countless secondary phase particles at the grain boundaries (Figure 3(e)), and the linear microstructure was therefore defined as the segregation band in the current study. The segregation band was complicated in chemical composition. The EDS analyses showed that it consisted of four phases (Table III), *i.e.*, Al-Cu-Mg-Fe-Mn, Al-Cu-Mn-Fe-Si, Al-Cu-Mg-Mn, and Al-Cu-Mg phases. It was noted that a number of segregation bands existed at the SDZ. Their patterns will be presented in Section III–B. In the PDZ, in contrast to the BM, most of the secondary phase particles were broken into smaller particles, and the linear microstructures were short and thin, and were therefore defined as short segregation bands in the current study (Figure 3(c)). In the SWZ, only a small number of secondary phase particles were broken up, and the microstructure was similar to that of the BM (Figure 3(d)).

Figures 4(a) and (b) show the backscattered SEM images of the SDZ of polished samples, H-800-100 and L-800-400. In contrast to the one in sample M-800-200, the segregation band was also clear in sample

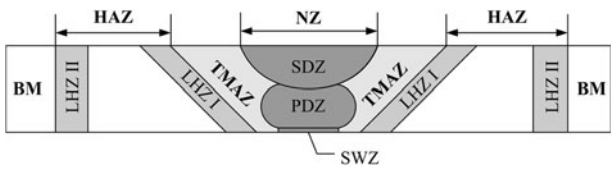

Fig. 2—A schematic of the transverse cross section of FSWed 2024Al-T351 joint, showing different sub-zones.

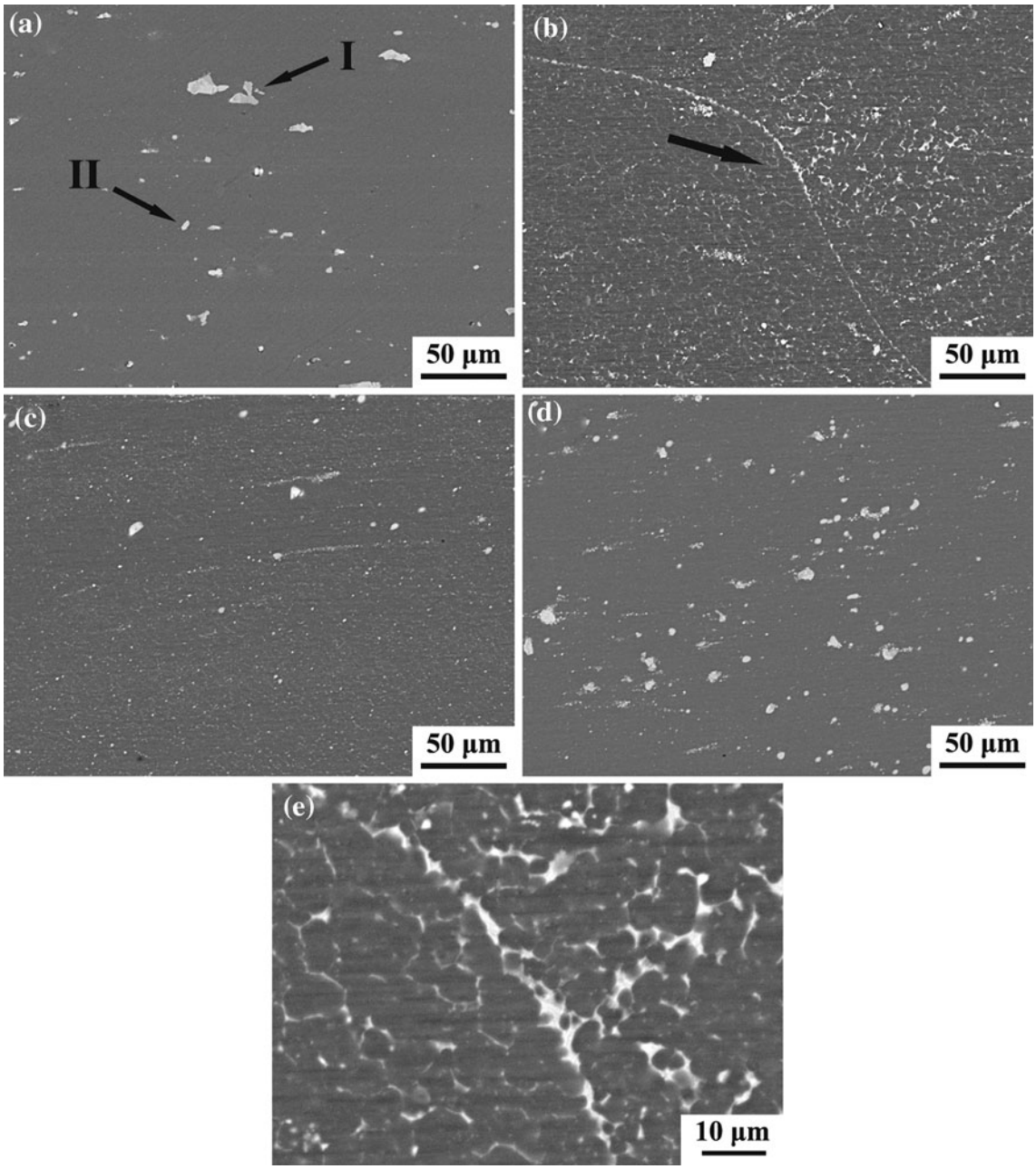

Fig. 3—SEM micrographs of polished sample M-800-200: (*a*) BM, (*b*) SDZ, (*c*) PDZ, (*d*) SWZ, (*e*) magnified micrograph of arrow zone in Fig. 3(b).

Table III. Chemical Composition of the Phases in BM and Segregation Bands (Weight Percent)

	BM		Segregation Bands			
Element	Large Phases I	Small Phases II	Phase III	Phase IV	Phase V	Phase VI
Al	54.21	44.24	66.46	41.08	67.80	66.22
Cu	26.29	39.71	24.17	25.58	24.56	28.23
Mg	—	16.06	3.35	—	5.08	5.55
Fe	9.88	—	2.73	9.94	—	
Mn	7.85	—	3.29	9.21	2.56	
Si	1.77	—	—	25.58	—	

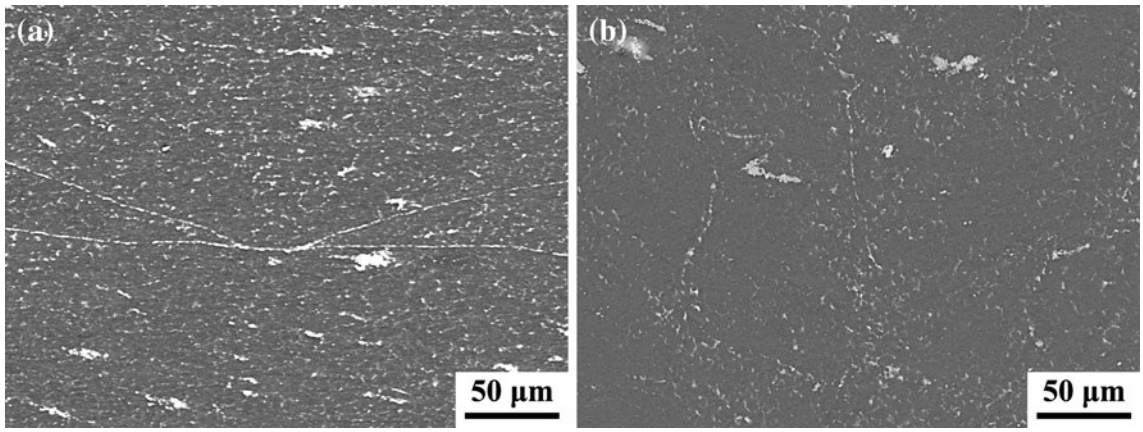

Fig. 4—SEM micrographs of SDZ in polished sample (*a*) H-800-100, and (*b*) L-800-400.

H-800-100, but was less distinct in sample L-800-400, indicating that the morphology of the segregation band was obviously dependent on the welding speed. It was noted that the segregation bands were very scarce and were observed in both SDZ and PDZ in sample L-800-400, which is illustrated in detail in Figure 5(c).

It should be pointed out that the "S" line could not be observed in the polished samples but was discernible by OM or SEM after etching.

B. *Distribution of Segregation Bands and "S" Line*

In the FSWed joint, the "S" line could be clearly observed by OM after etching with 2 pct NaOH aqueous solution.[20] Meanwhile, the segregation bands become clearer under OM, which made it possible to simultaneously observe their distributions in the FSWed 2024Al-T351 joints. However, both the "S" line and segregation bands were very thin and could be clearly observed only in the micrographs. So, in the current study, composite images of the joints consisting of about 100 microscopic images were produced in which the segregation bands and "S" line were plotted as black solid and dotted lines, respectively, and then the composite images were zoomed out to a standard size for macro-observation. The current study was less concerned with the short segregation bands in the PDZ, which were very short and unclear.

1. *Segregation bands and "S" line patterns on the transverse cross section*

Figures 5(a) through (c) show the macroscopic patterns of samples H-800-100, M-800-200, and L-800-400, respectively. It can be seen that for the three samples the size of the SDZ gradually shrunk, while the sizes of the PDZ and SWZ enlarged as the welding speed increased from 100 to 400 mm min^{-1}. The variational tendencies of the SDZ, PDZ, and SWZ were in agreement with the results reported by Arbegast,[29] who found that the patterns of the NZ were dependent on the welding parameters.

In sample H-800-100, the segregation bands of varied lengths, magnified images of which are shown in Figure 5(d), were distributed at different depths of the SDZ (Figure 5(a)). The individual segregation bands started from the RS top surface of the joint, ran down to a certain depth in the middle of the SDZ, and then ran up to the AS top surface. They were basically axisymmetric. No obvious "S" line was observed, which is in agreement with the finding of Sato *et al.*[20] that the "S" line was not clear in the high weld pitch (high plastic deformation) FSWed joint.

Compared with the segregation bands in sample H-800-100, those in sample M-800-200 were much fewer in number and were a little denser on the RS than those on the AS (Figure 5(b)). The magnified image is shown in Figure 5(e). At the bottom of the joint, the "S" line started from the bottom of the centerline, deviated upward to the RS along the PDZ/TMAZ interface, and became unclear near the middle position.

When the welding speed was further increased to 400 mm min^{-1}, the intact "S" line was present in sample L-800-400 (Figure 5(c)). It can be seen that the "S" line was similar to that of sample M-800-200 at the bottom (the magnified image is shown in Figure 5(f)), but it then extended jaggedly toward the AS and finally extended upward to the top of the joint. Three different zones were discernible in the PDZ, that is, I, II, and III, respectively. Zone III corresponded to the onion rings and was on the right of the "S" line, which is in agreement with the result of Xu and Deng.[32] Unlike samples H-800-100 and M-800-200, in which the segregation bands existed only at the SDZ, the segregation bands were observed in both the SDZ and the PDZ of sample L-800-400. In the SDZ, they were mainly located at the RS interface of SDZ/TMAZ (marked by arrow G; the magnified SEM image is shown in Figure 4(b)). In the PDZ, they were connected with the segregation bands at the RS interface of SDZ/TMAZ and extended downward along the interface of zones I/II (Figure 5(c)).

2. *Segregation bands and "S" line patterns on the longitudinal cross section*

Figure 6 shows the distribution of the segregation bands and "S" line on the longitudinal cross sections of the three samples, which could be correlated with those on the transverse cross section to provide their clear overall patterns.

In sample H-800-100, the sloping segregation bands, which had a horizontal angle of about 26 to 28 deg and

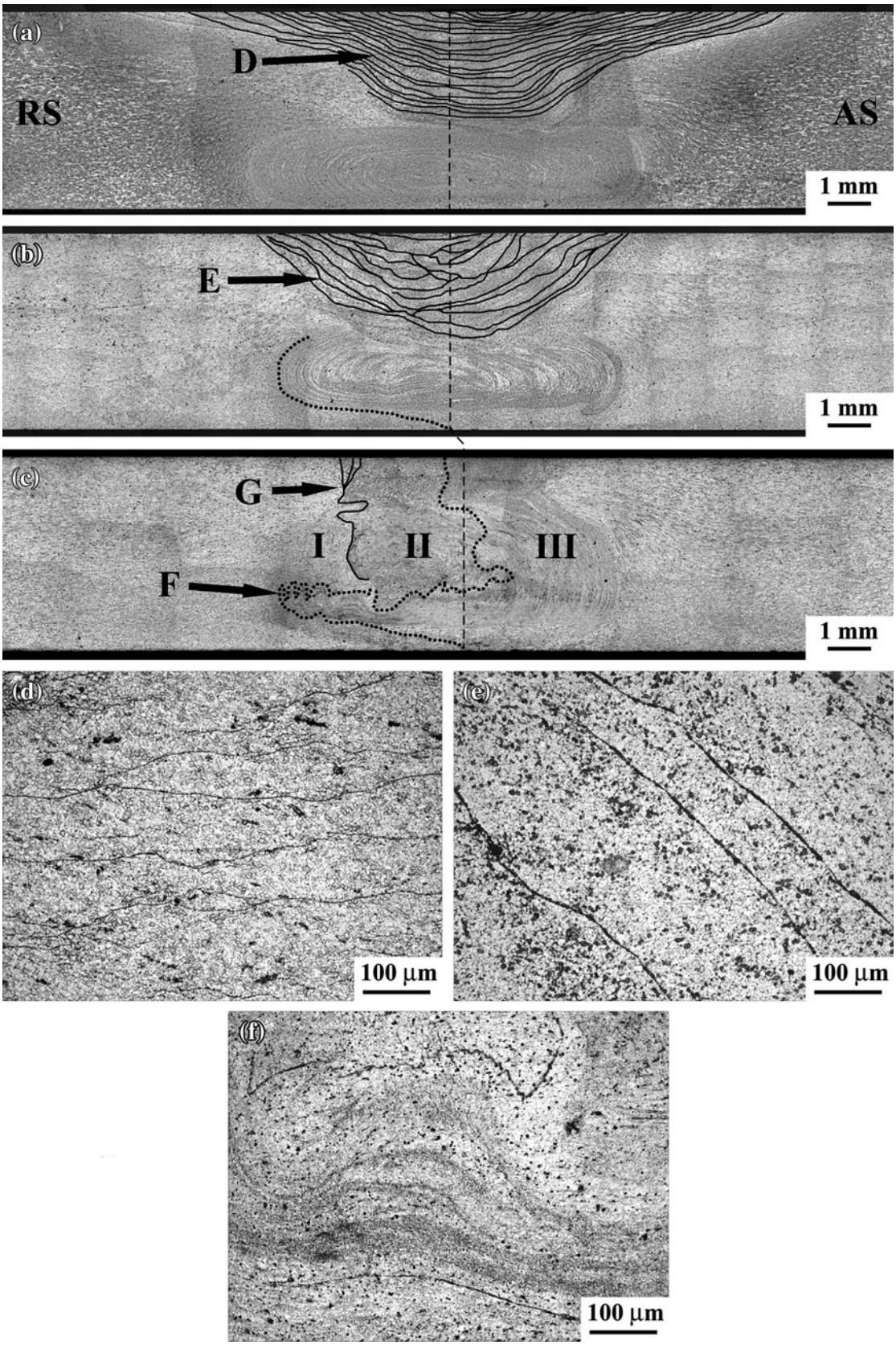

Fig. 5—Segregation bands and "S" line patterns on transverse cross sections of (*a*) sample H-800-100, (*b*) sample M-800-200, and (*c*) sample L-800-400; (*d*), (*e*), and (*f*) magnified micrographs of positions D, E, and F as shown in Figs. 5(a) through (c), respectively (the AS is on the right). The vertical dashed line in Figs. 5(a) through (c) represents the weld center.

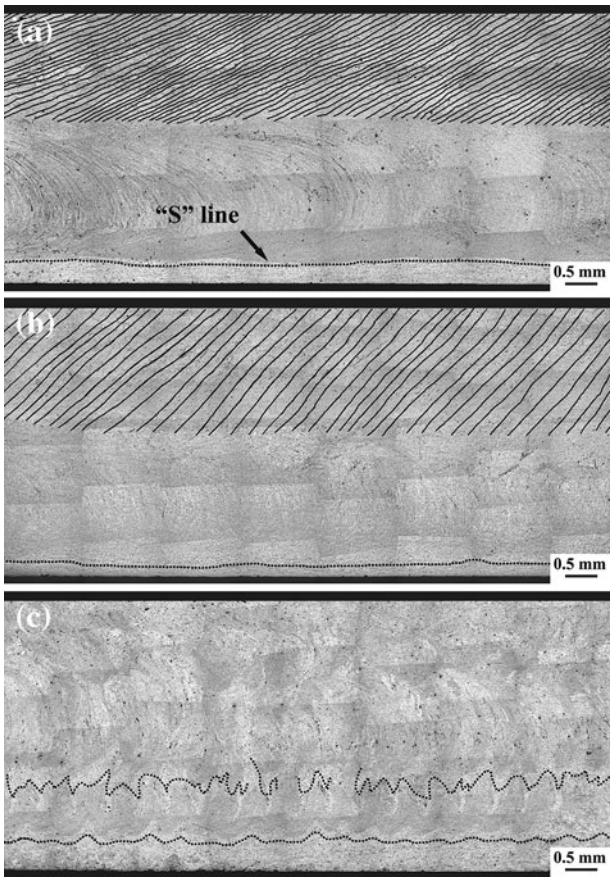

Fig. 6—Segregation bands and "S" line patterns on longitudinal cross sections of (*a*) sample H-800-100, (*b*) sample M-800-200, and (*c*) sample L-800-400 (The welding direction is from right to left).

were generally parallel to each other, extended from the top of the joint to the bottom of the SDZ (Figure 6(a)). The average band spacing was about 0.12 to 0.13 mm and close to the tool advancement per revolution ($V/R = 0.125$). In the PDZ, semicircular structures were observed, which corresponded to the pattern of onion rings on the transverse cross section. The "S" line (marked by an arrow) was continuous and smooth on this cross section.

The pattern of the segregation bands in sample M-800-200 (Figure 6(b)) was similar to that in sample H-800-100, but the horizontal angle was about 42 to 45 deg, and the average band spacing was about 0.2 to 0.3 mm and close to the tool advancement per revolution ($V/R = 0.25$). In the PDZ, the degree of bending of onion rings was smaller. The feature of the "S" line at the bottom was unchanged.

Unlike the smooth "S" lines in Figures 6(a) and (b), two wavy "S" lines, one with a large amplitude in the PDZ and the other with a small amplitude in the SWZ, were observed in sample L-800-400 (Figure 6(c)), which corresponded to the "S" line at the centerline position on the transverse cross section in Figure 5(c). It should be noted that no obvious segregation band was observed on this cross section of sample L-800-400.

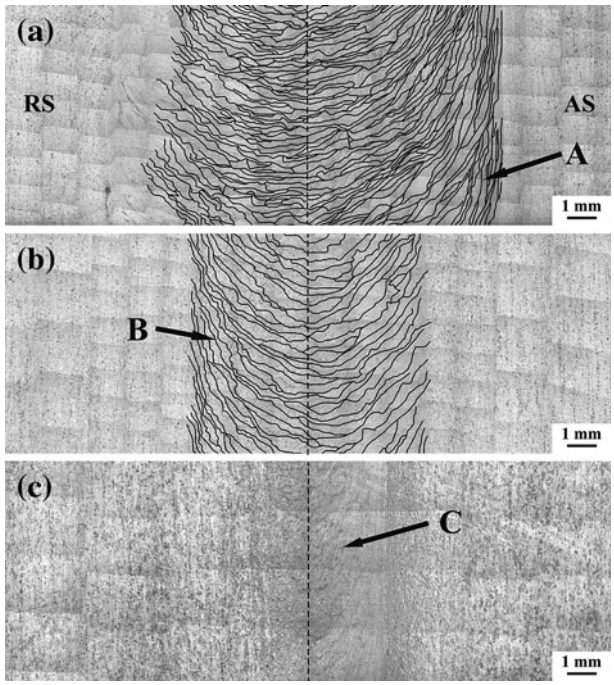

Fig. 7—Segregation bands patterns on horizontal cross section of (*a*) sample H-800-100, (*b*) sample M-800-200, and (*c*) sample L-800-400 (the AS is on the right). The vertical dashed line represents the weld centerline before welding.

3. *Segregation bands and "S" line patterns on the horizontal cross section*

Figure 7 shows the macrographs of the horizontal cross sections at the top of the three samples. The magnified images of the representative details of positions A, B, and C are shown in Figures 8(a) through (c), respectively. On this section, the "S" line was invisible for all the samples. In the samples H-800-100 and M-800-200, the semicircular segregation bands were observed (Figures 7(a) and (b) and 8(a) and (b)). Consistent with those on the longitudinal cross sections, their average band spacing was also found to be approximately equal to the tool advancement per revolution. In sample L-800-400, the segregation bands could not be observed (Figure 7(c)), but the magnified image of the arrow zone (Figure 8(c)) showed the regular directional distribution of the secondary phase particles (the black particles).

C. *Manmade Oxide Film and Tool Extraction Weld*

Figure 9 shows the macrograph of the horizontal cross section of sample M-800-200 prepared by means of the manmade oxide film and tool extraction technologies. The butting surfaces deviated to the RS in front of the pin, bypassed the pin in a semicircular path, and finally became parallel to the welding direction out of the shoulder. This indicates that the butting surfaces did not make contact with the rotating pin during FSW and evolved directly into the "S" line without a change in chemical composition.

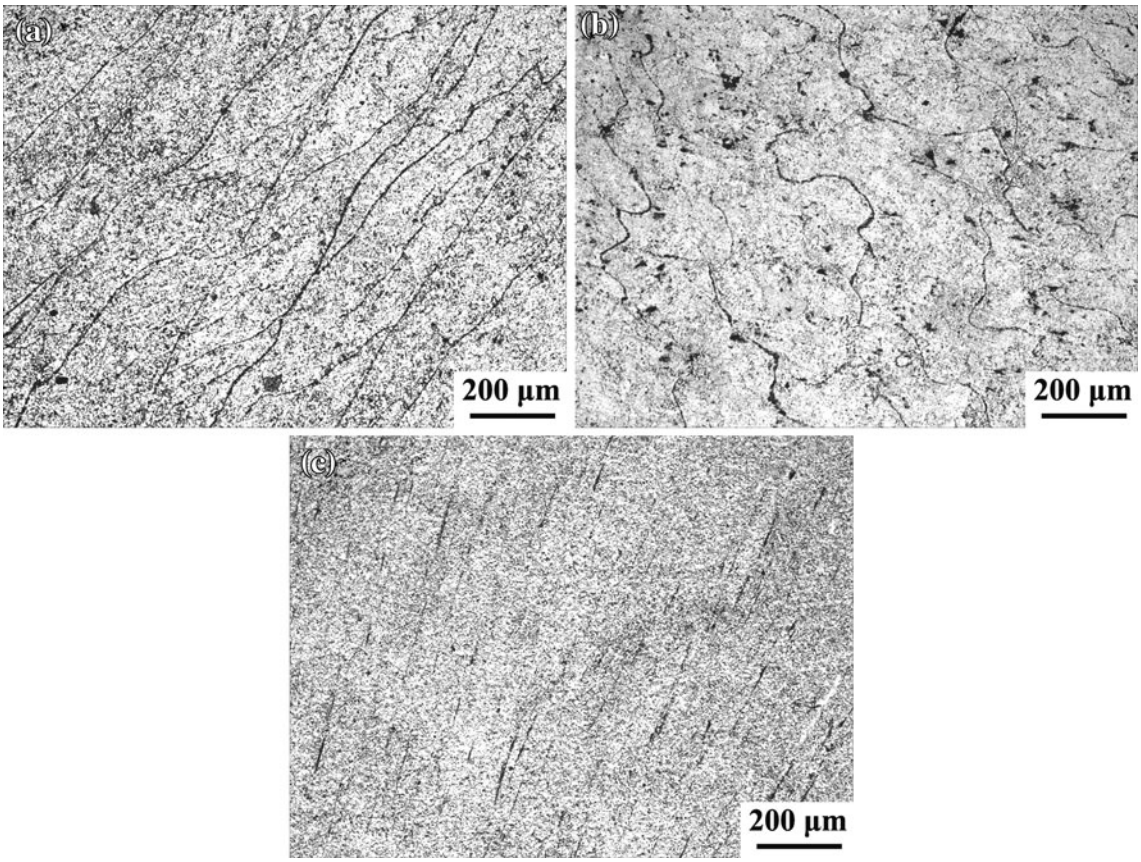

Fig. 8—Magnified OM micrographs of positions A, B, and C as shown in Figs. 7(a) through (c), respectively.

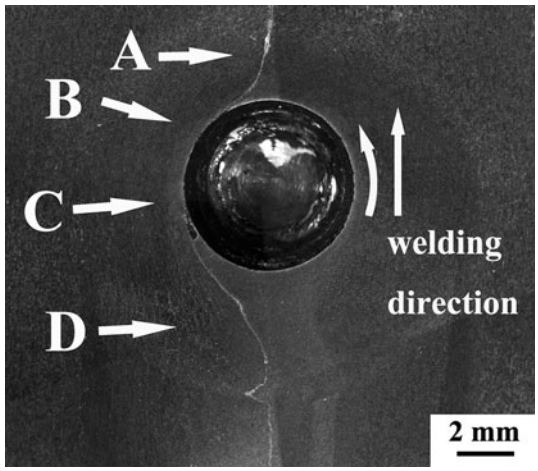

Fig. 9—The horizontal cross section of sample M-800-200 prepared by manmade oxidation film and tool extraction technologies (etched with 2 pct NaOH aqueous solution; the AS is on the right).

With regard to the segregation bands, four representative positions A, B, C, and D on their evolutionary path are marked by the arrows (Figure 9). The magnified secondary electron SEM images of four positions showing the evolution of secondary phase particles are presented in Figures 10(a) through (d), respectively, and their corresponding magnified OM micrographs showing the evolution of grain structures are provided in Figures 10(e) through (h), respectively. The white phases or segregation bands in Figures 10(a) through (d) corresponded to the black ones in Figures 10(e) through (h).

At position A ahead of the advancing pin, the distribution of secondary phase particles was similar to that in the BM and the grains had a length of 100 to 200 μm and width of approximately 20 to 50 μm (Figures 10(a) and (e)). At position B close to the pin, the secondary phase particles were assembled in bands with the normal direction pointing to the center of the keyhole, and the elongated coarsened grains were more than 400 μm in length and approximately 20 to 50 μm in width (Figures 10(b) and (f)). At position C, the secondary phase particles were broken up, forming many unclear short linear structures at the grain boundaries, and the fine elongated grains were much smaller than those at position B (Figures 10(c) and (g)). At position D behind the pin, the clear segregation bands formed, and the fine equiaxed and coarse grains could be observed (Figures 10(d) and (h)). It could be inferred that the position of the segregation bands would alter and the grain structures at position D would further evolve into the microscale grains until the shoulder passed.

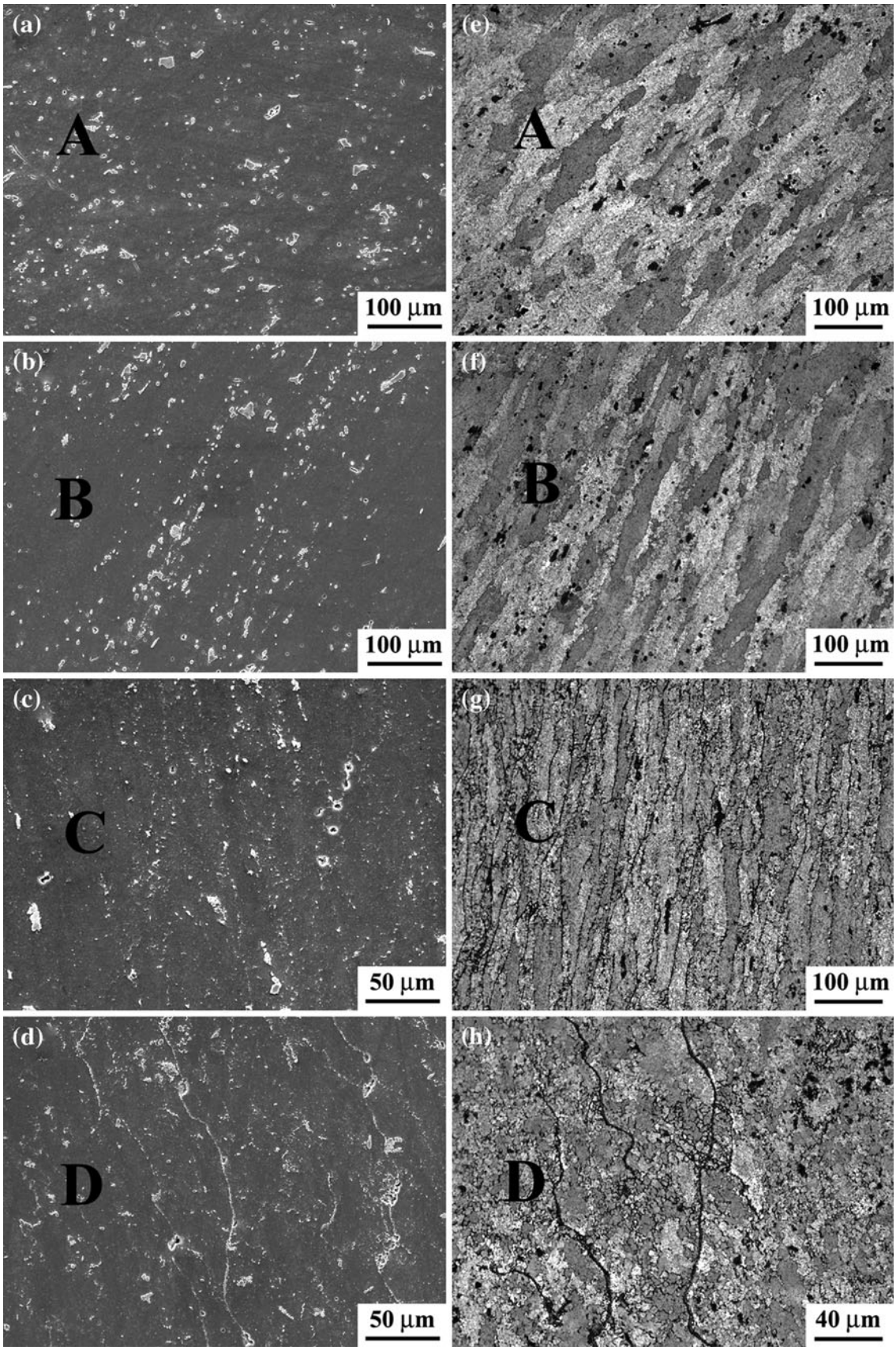

Fig. 10—Magnified micrographs of Fig. 9 from position A to position D: (*a*) through (*d*), SEM images showing evolution of secondary phase particles (etched with Keller's reagent); (*e*) through (*h*), OM images showing evolution of grain structure (etched with 2 pct NaOH aqueous solution).

D. *Microhardness Profile*

Figure 11 shows the microhardness profiles of samples H-800-100, M-800-200, and L-800-400. The double "W" shaped hardness profiles exhibited two LHZs on both RS and AS of the joints. The LHZs near and far from the NZ were defined as LHZ I and LHZ II, respectively, in the current study (marked in Figure 11). It can be found that as the welding speed increased from 100 to 400 mm min^{-1}, the hardness of LHZ I increased gradually, while the hardness of LHZ II essentially unchanged, and the locations of LHZ I and LHZ II moved inward to the centerline of the joint. It should be noted that the relationship between LHZ I and welding speed of FSWed 2024Al-T351 joint in the current study was in agreement with that of FSWed joints of 6061Al-T651,[6,7] 7010Al-T7651,[33] and 7050Al-T7451.[34]

On the other hand, the hardness of the NZ was basically unchanged with the welding speed and was slightly lower than that of the BM. It is noted that the hardness of LHZ I was lower than that of LHZ II in samples H-800-100 and M-800-200 but was slightly higher than that of LHZ II in sample L-800-400.

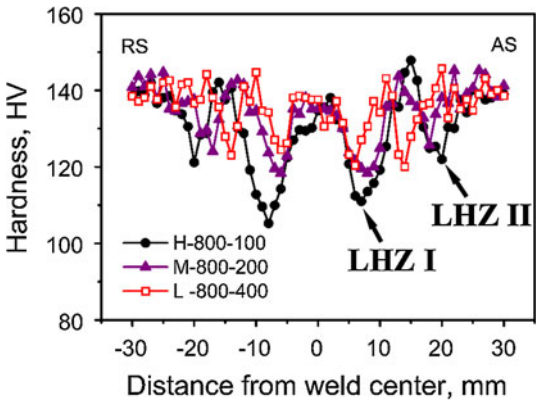

Fig. 11—Hardness profiles of FSWed 2024Al-T351 joints.

E. *Fracture Location and Morphology*

Figures 12(a) through (e) show the five typical fracture locations of the three samples, which were defined as fractures I, II, III, IV, and V, respectively. Fracture I occurred in sample H-800-100 and was along LHZ I on the RS (Figure 12(a)), which was in good agreement with the typical fracture locations of FSWed precipitation-hardened Al alloy joints.[6,7,35] Fractures II and III occurred in sample M-800-200 (Figures 12(b) and (c)). The fracture path of fracture II was along the segregation bands at the middle of the SDZ and then diagonally across the PDZ. It is noted that a crack was produced at the RS interface of NZ/TMAZ of sample M-800-200 during tension (Figures 12(b)). The fracture path of fracture III was along the segregation bands at the RS interface of SDZ/TMAZ at the top and crossed the PDZ obliquely at the bottom (Figures 12 (c)), which was similar to the fracture characteristic of the FSWed 7075Al joint in Reference 26. It was worth noting that fracture II rarely occurred and most of the fracture cases were fracture III. Fractures IV and V occurred in sample L-800-400 (Figures 12(d) and (e)). The fracture path of fracture IV originated along the segregation bands at the top and extended to the RS at the bottom. Fracture V was located in LHZ II on the RS.

Figures 13 and 14 show the typical SEM fractographs for fractures I, III, IV, and V. The macroscopic images of the usual fractures I and V that corresponded to the LHZs show the flat fracture surfaces (Figures 13(a) and (b)). The magnified images of positions A and B show the mixed fracture at fracture I and the ductile rupture at fracture V, respectively (Figures 14(a) and (b)). The unusual fractures III and IV corresponded to neither LHZ I nor LHZ II, and therefore deserved more attention. Their macroscopic SEM fracture surfaces are shown in Figures 13(c) and (d), respectively. It can be seen that their upper parts with step-like fracture surfaces were clearly different from the flat surface of their lower parts. The microscopic images show the transgranular fracture at their upper positions C and E (Figures 14(c) and (e)), while the cleavage fracture occurred at their lower positions D and F (Figures 14(d) and (f)).

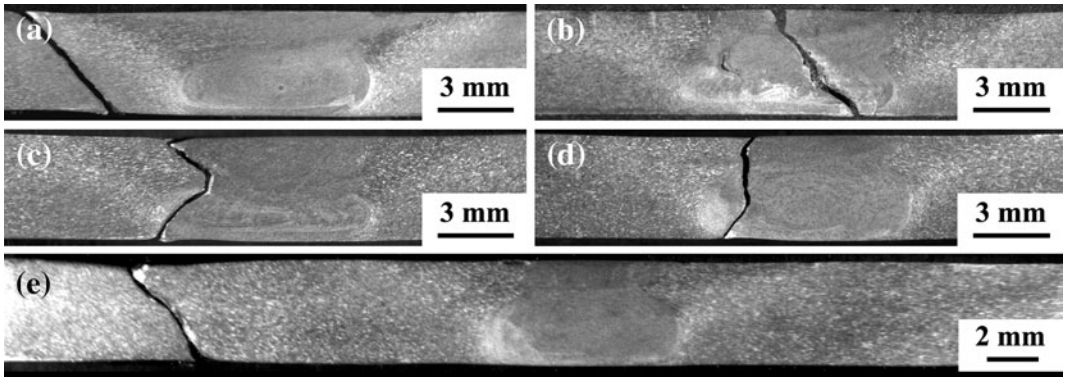

Fig. 12—Typical fracture mode of FSWed 2024Al-T351 joints: (*a*) fracture I of sample H-800-100; (*b*) fracture II and (*c*) fracture III of sample M-800-200; (*d*) fracture IV and (*e*) fracture V of sample L-800-400 (the AS is on the right).

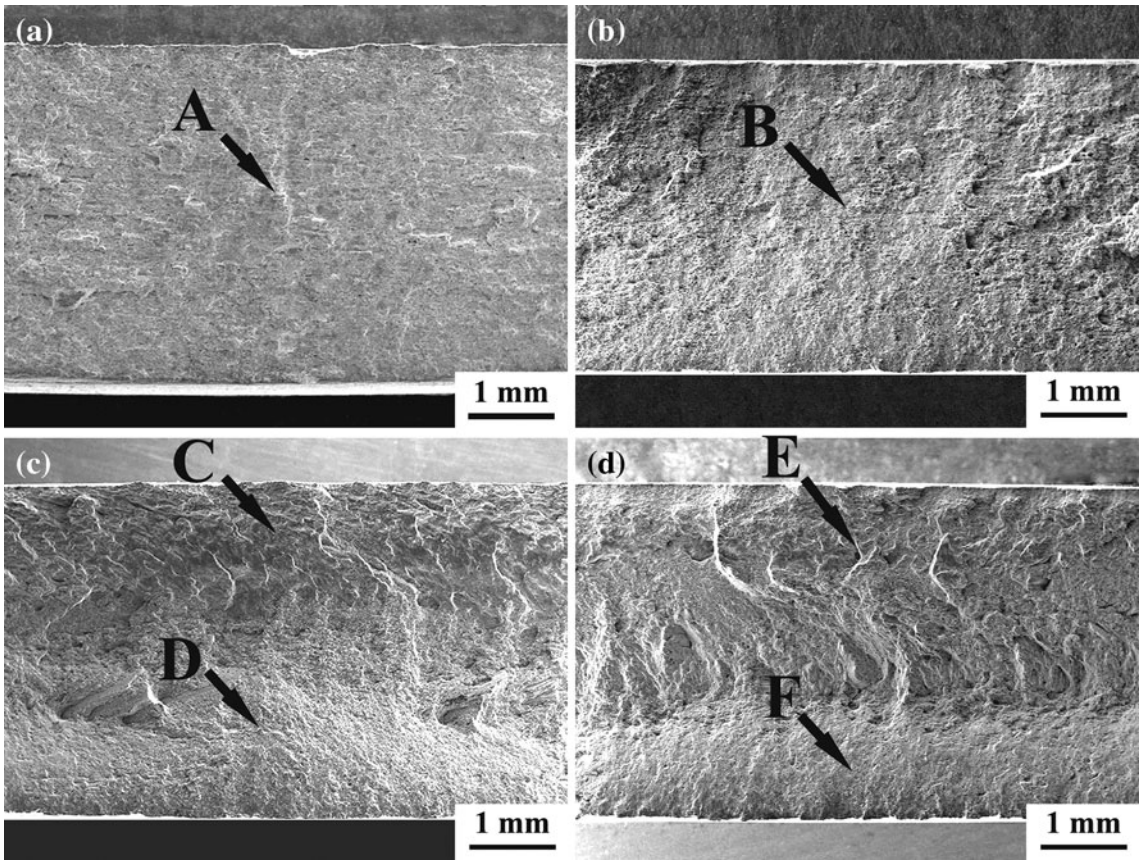

Fig. 13—Macrographic fractographs of (*a*) fracture I, (*b*) fracture V, (*c*) fracture III, and (*d*) fracture IV.

IV. DISCUSSION

All of the above results indicate that the formation of the segregation bands and "S" line was closely related to the material flow during FSW, and they were obviously different in morphology, chemical composition, and distribution, indicating their different formation mechanisms. It was indicated that the segregation bands resulted in the unusual fracture behavior of the FSWed 2024Al-T351 joints.

A. *Formation of "S" Line and Segregation Bands During FSW*

1. *Formation of "S" line*

The butting surfaces evolved into the "S" line in a simple way. With the forward and anti-clockwise rotation of the welding tool, the butting surfaces moved along a semicircular path (Figure 9). Under the high temperature and large plastic deformation, the two plates were joined together, and the butting surfaces evolved into the "S" line. The continuity of the "S" line was dependent on the degree of plastic deformation.[20] The low welding speed of 100 mm min^{-1} led to a long stirring time per unit length, producing the wide and diluted distribution of the oxide film. Thus, the "S" line was not distinct on the transverse cross section (Figure 5(a)) and was only clear on the longitudinal cross section of sample H-800-100 (Figure 6(a)). In sample M-800-200, the plastic deformation was smaller than that in sample H-800-100 because of the increase in the welding speed. In this case, the "S" line was indistinguishable in the SDZ with a large plastic deformation, and only a part of the "S" line was observed in the PDZ where a small plastic deformation took place (Figure 5(b)). When the welding speed was increased from 200 to 400 mm min^{-1}, the plastic deformation decreased further, making the oxide film denser and more continuous. The intact "S" line was therefore observed in both SDZ and PDZ in sample L-800-400 (Figure 5(c)).

2. *Formation of segregation bands*

During FSW, intense plastic deformation and frictional heating result in the redistribution of secondary phase particles in the NZ. It should be noted that, in the BM, the large sharp edge of Al-Cu-Mn-Fe-Si phase indicated that the Al-Cu-Mn-Fe-Si phase did not dissolve whereas the smooth edge of Al_2CuMg phase particles showed that part of Al_2CuMg phase remained during the solution heat treatment at 775 K (502 °C). In the NZ, the peak temperature was about 773 K to 823 K (500 °C to 550 °C),[36,37] indicating that the dissolution and break up of secondary phase particles occurred during FSW. Thus, the distribution of secondary phase particles was closely related with frictional heating and material flow induced by the plastic

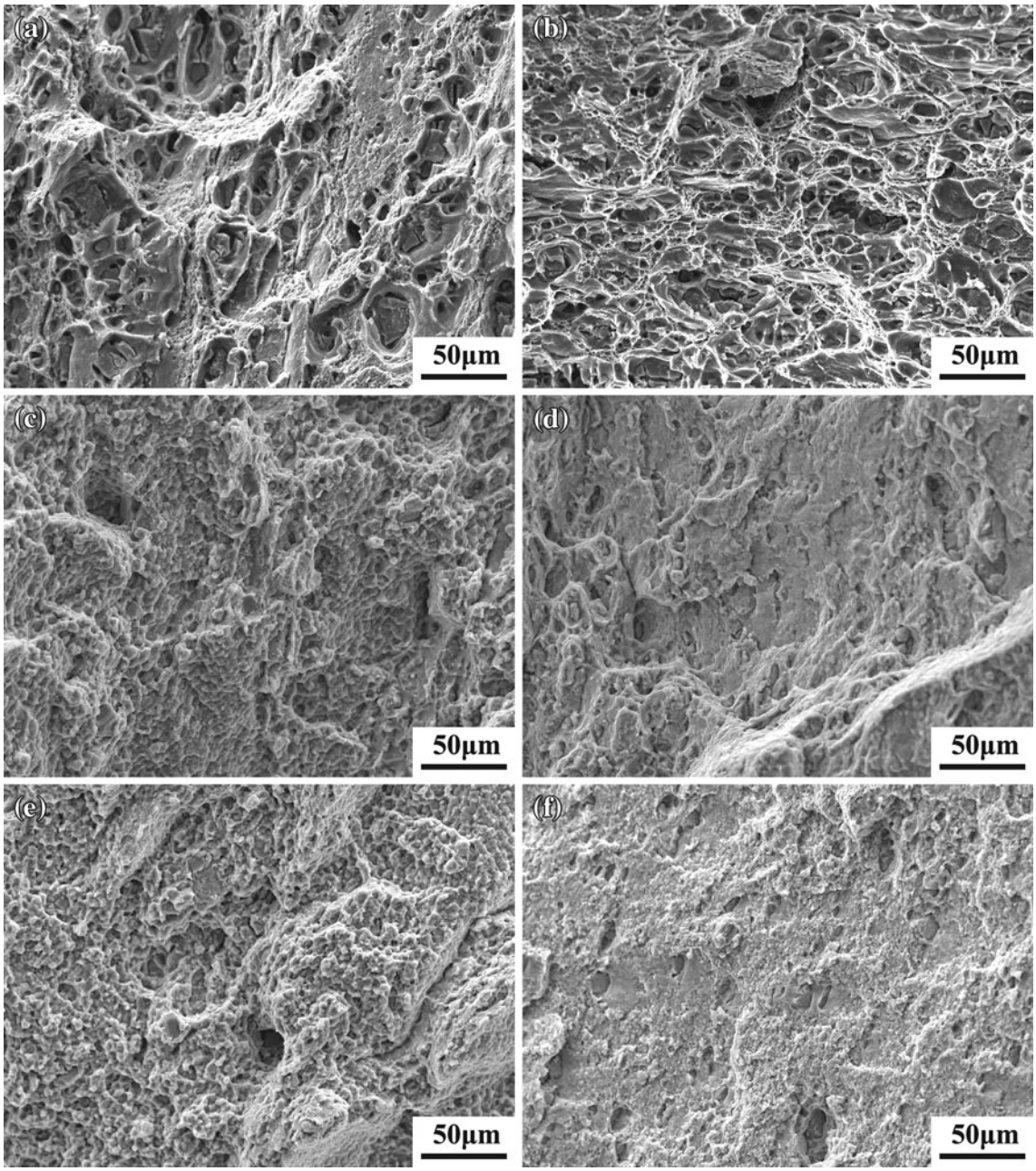

Fig. 14—Magnified micrographs of Fig. 13 from position A to position F: (*a*) position A, (*b*) position B, (*c*) position C, (*d*) position D, (*e*) position E, and (*f*) position F.

deformation during FSW. The general formation process of segregation bands could be explained as follows.

To put it simply, during FSW, the material flow was a periodic process and the welding tool rotated a circle at one period.[18–39] During one period, the material flow was an inhomogeneous process, the stress state and torque varied as the welding tool changed its relative position during one revolution.[39,40] The periodic and inhomogeneous material flow resulted in large strain and strain rate gradients.[41,42] The secondary phase particles tended to aggregate at the region of high strain rate gradient,[20] thereby forming the bands of secondary phase particles (Figure 10(b)). During the subsequent process, the secondary phase particles were broken up and aggregated at the specific region, evolving into the segregation bands. It should be noted that, probably because the temperature and strain rate gradient in the PDZ were more suited for the redistribution of secondary phase particles than those in the SDZ, the segregation bands in the SDZ were longer and more continuous than those in the PDZ.

Based on Figures 9 and 10, the detailed evolution of the secondary phase particles into the segregation bands could be described as follows. It is noted that the

formation of the segregation bands and the recrystallization occurred simultaneously and correlated with each other during FSW.

(i) The evolution of secondary phase particles and grain structures is strongly related with the strain and temperature. In the initial deformation area (position A in Figure 9) with the low strain and temperature, the secondary phase particles and grain structures were almost identical to those in the BM (see Figures 10(a) and (e)).
(ii) As the strain and temperature increased (position B in Figure 9), the secondary phase particles aggregated at the region of high strain rate gradient along the shear material flow direction, *i.e.*, the rotation direction of the welding tool, forming the particle aggregation bands (Figure 10(b)). The grains coarsened and the grain boundaries rotated toward the shear material flow direction, forming the elongated coarse grains because of the geometric requirements of strain (Figure 10(f)).
(iii) Under further increased strain and temperature (position C in Figure 9), most of the secondary phase particles (phases I and II) in the particle aggregation bands were broken up, and partially dissolved (see Figure 10(c)). At the same time, based on the original grain boundaries of the elongated coarse grains, the elongated coarse grains were subdivided into finer elongated grains[43] (see Figure 10(g)).
(iv) The trend of the particle breaking up and grain refinement (to microscale) was further enhanced under continued plastic deformation and heat input (position D in Figure 9). During this process, the recrystallization progress was prevented by the particle phases, and the small secondary phase particles recombined at the grain boundaries, forming continuous segregation bands consisting of four types of secondary phase particles (see Figure 3(e), 10(d), and (h); Table III).
(v) The segregation bands would move until they got rid of the drive of the shoulder. In other words, the final position of the segregation bands corresponded to the profile of the SDZ, which will be discussed in detail in the next section.

B. *Pattern of Segregation Bands in Different FSWed Joints*

The inhomogeneous material flow resulted in the formation of one segregation band during one revolution. The periodic material flow led to the onion ring structure in the PDZ and the fluctuating surface pattern of the FSWed joint.[41] In the current study, the periodic variation of material flow also affected the distribution of the segregation bands.

The FSW process is shown schematically in Figure 15(a). The segregation bands mainly formed in the SDZ and the pattern of the segregation bands was identical to the profile of the SDZ. The shape of the SDZ was dependent on the welding parameters, plunge depth and welding tool. In order to facilitate calculation, it is assumed that the SDZ during FSW is a semicircular truncated cone in the current study, as shown in Figure 15(b). In this case, the curved surface ABC–A′B′C′ corresponds to the segregation band and the ladder-shaped cross section AC–A′C′ corresponds to the transverse cross section of the SDZ (Figure 15(c)).

The pattern of the segregation bands on the horizontal cross section (X-O-Y) could be described by the periodic equation proposed by Cui *et al.*[41]

$$\begin{aligned} y &= r\cos\omega t_{\mathrm{m}} \\ x &= (vt_{\mathrm{m}} - r\sin\omega t_{\mathrm{m}})\cos\alpha \quad t_{\mathrm{m}} = t + 2(n-1)\pi/\omega, \\ & 0 \le t \le \pi/\omega,\ n = 1, 2, 3\ldots \end{aligned} \tag{1}$$

where x and y are the coordinates of the pattern, v (mm s^{-1}) is the travel speed of the tool, t_{m} (s) is the time taken for the formation of the nth segregation band, r (mm) is the radius of the SDZ, ω (rad s^{-1}) is the angular velocity of the tool, and α (degrees) is the tilt angle of the welding tool.

On the transverse cross section of the SDZ (Y-O-Z), as illustrated in Figure 15(c), the coordinate z (mm) of the pattern can be expressed as

$$z = h(r_1 - r)/(r_1 - r_2) \quad (r_2 \le r \le r_1) \tag{2}$$

where r_1 (mm) is the radius of the SDZ at the top, r_2 (mm) is the radius of the SDZ at the bottom, r (mm) is the radius of the SDZ at coordinate z, and h (mm) is the height of the SDZ.

It should be noted that the angle β between the top surface and the side surface corresponds to the horizontal angle of the segregation bands on the longitudinal cross section of the FSWed joint, which can be expressed as

$$\cos\beta = (r_1 - r_2) \Big/ \sqrt{(r_1 - r_2)^2 + h^2} \tag{3}$$

The time t_r (s) taken for the tool to make one revolution is

$$t_r = 2\pi/\omega \tag{4}$$

Substituting Eq. [4] into Eq. [1], we obtain the spacing between two adjacent semicircular lines along the y direction as

$$D = v \cdot (2\pi/\omega) \cdot \cos\alpha \tag{5}$$

Considering that α is small, so that $\cos\alpha \approx 1$, then substituting $\omega = R \cdot 2\pi/60$ and $v = V/60$ into Eq. [5],

$$D = v \cdot (2\pi/\omega) = V/R \tag{6}$$

where V (mm min^{-1}) is the welding speed, and R (rpm) is the rotation rate.

According to Eqs. [1], [2], [3], and [6], the ideal patterns of the segregation bands in the FSWed 2024Al-T351 joints could be generally described.

It should be noted that the segregation bands were not parallel but interconnected with each other because the

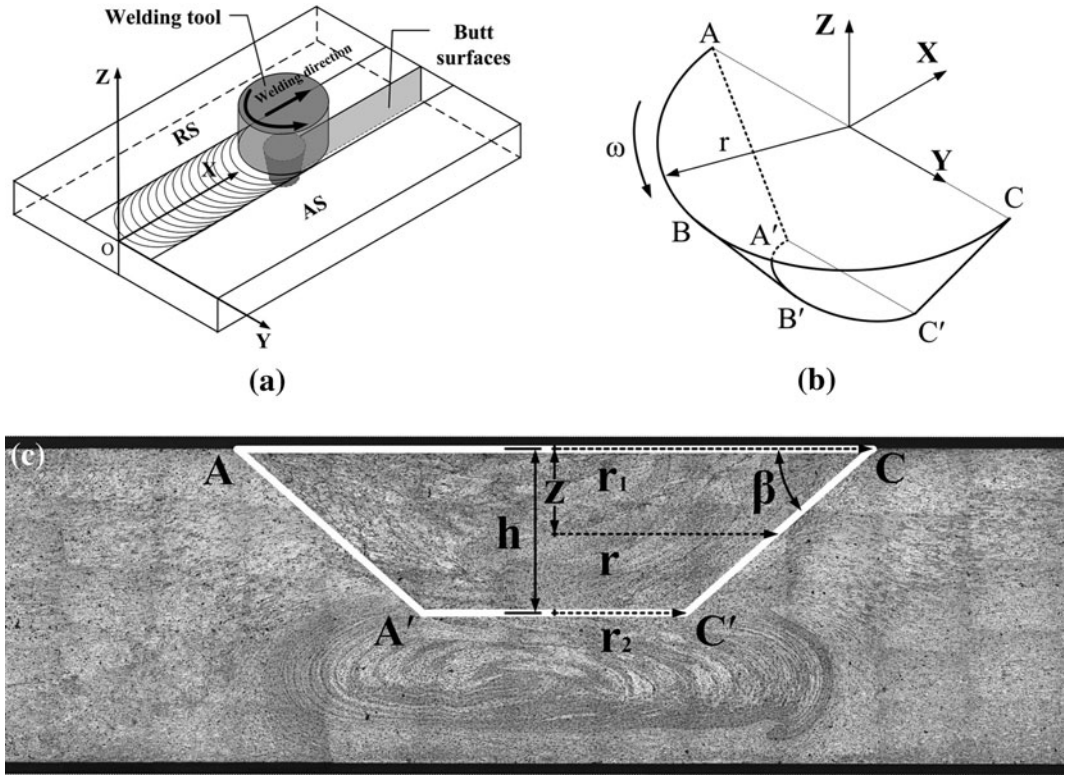

Fig. 15—Schematics showing essential material flow details: (*a*) welding process, (*b*) shape of SDZ, and (*c*) shape of SDZ on transverse cross section in sample M-800-200.

Table IV. Comparison Between Experimental and Calculated Band Spacing of Segregation

	Band Spacing (mm)	
Sample	Experimental	Calculated
H-800-100	0.12 to 0.13	0.125
M-800-200	0.2 to 0.3	0.25
L-800-400	—	—

long straight grain boundaries were interrelated with each other. Thus, the predicted patterns of the segregation bands may not be in complete agreement with the observed experimental patterns. The comparison between the experimental and calculated band spacings of the segregation bands is shown in Table IV.

1. *Sample H-800-100*

In the sample H-800-100, $\omega \approx 26.67\pi$ rad s^{-1}, $v \approx 1.67$ mm s^{-1}, $\alpha = 2.75$ deg, $r_1 = 12.7$ mm, $r_2 = 3.2$ mm, and $h = 2.3$ mm. Substituting these parameters into Eqs. [1], [2], [3], and [6], respectively, the predicted patterns of the segregation bands are shown in Figure 16. The theoretical spacing of the segregation bands is determined to be 0.125 mm. It is found that the predicted curves generally fit the patterns of the segregation bands on the 3D cross sections of sample H-800-100 (Figures 5(a), 6(a), and 7(a)).

2. *Sample M-800-200*

In sample M-800-200, $\omega \approx 26.67\pi$ rad s^{-1}, $v \approx 3.33$ mm s^{-1}, $\alpha = 2.75$ deg, $r_1 = 8.2$ mm, $r_2 = 3.5$ mm, and $h = 2.1$ mm. Substituting these parameters into Eqs. [1], [2], [3], and [6], respectively, the theoretical spacing of the segregation bands is calculated to be 0.25 mm. The predicted curves also generally fit the patterns of the segregation bands on the 3D cross sections of sample M-800-200 (Figures 5(b), 6(b), and 7(b)).

3. *Sample L-800-400*

In sample L-800-400, the high welding speed of 400 mm min^{-1} produced a very short stirring time per unit length, leading to the low heat input and insufficient material flow.[28] And the only method of avoiding defects induced by the insufficient material flow was to increase the plunge depth to force more RS material to take part in the formation of weld. This resulted in great changes in material flow. During this process, no stable SDZ formed because of the change in the material flow. In the SDZ, the weakening in heat input and material flow resulted in a decrease in the number and thickness of the segregation bands (Figure 4(b)). The segregation bands only formed near the RS interface of SDZ/TMAZ in the SDZ (Figure 5(c)). In the PDZ, the less deformed RS material formed zone I and the severely deformed RS material formed zone II (Figure 5(c)). A large strain rate gradient occurred along the interface of zones I and

II, resulting in the formation of the segregation band in the PDZ (a magnified SEM image is shown in Figure 17), which was connected with the segregation bands at the SDZ/TMAZ interface (Figure 5(c)).

C. *Effect of Segregation Bands on the Fracture Behavior of FSWed Joints*

In general, the FSWed joints of precipitation-hardened aluminum alloys fractured along the LHZs of the HAZs on the transverse tension.[6,7] Figure 11 show that at all three welding speeds, the hardness of the LHZs was much lower than that of the NZ. However, the FSWed 2024Al-T351 joints did not always fracture along the LHZs (Figure 12). This indicates that the segregation bands weakened the mechanical properties of the local regions (NZ and SDZ/TMAZ interface), thereby changing the tensile fracture behavior of the FSWed 2024Al-T351 joints at welding speeds of 200 and 400 mm min^{-1}.

From Figures 5, 11, and 12, it is clear that whether the segregation bands affected the fracture behavior of the FSWed 2024Al-T351 joints was dependent on the competition between the hardness value of the LHZs and the density of the segregation bands. Sample H-800-100 fractured along LHZ I because the hardness of LHZ I was much lower than that of the NZ (Figure 11), in spite of higher density of the segregation bands in the NZ (Figure 5(a)).

Increasing the welding speed from 100 to 200 mm min^{-1} resulted in the reduction in both the hardness gap between NZ and LHZ I (Figure 11) and the density of the segregation bands in sample M-800-200 (Figure 5(b)). In this case, the segregation bands played a role, resulting in the unusual fracture behavior of the joint along the segregation bands. The zone with the dense segregation bands was generally located at the RS interface of NZ/TMAZ (Figures 5(b) and 7(b)) and

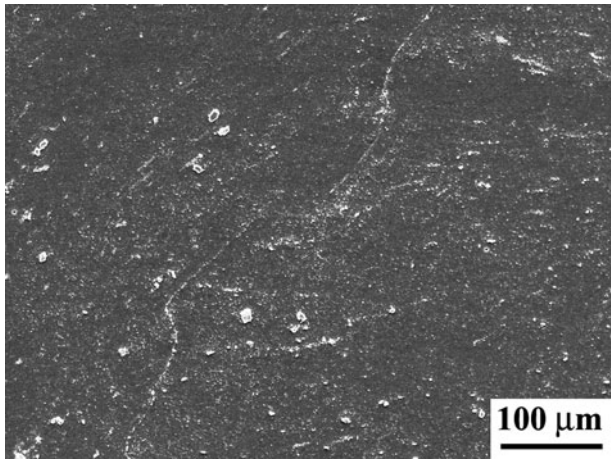

Fig. 17—Segregation bands at the interface of zones I/II of sample L-800-400 as shown in Fig. 5(c).

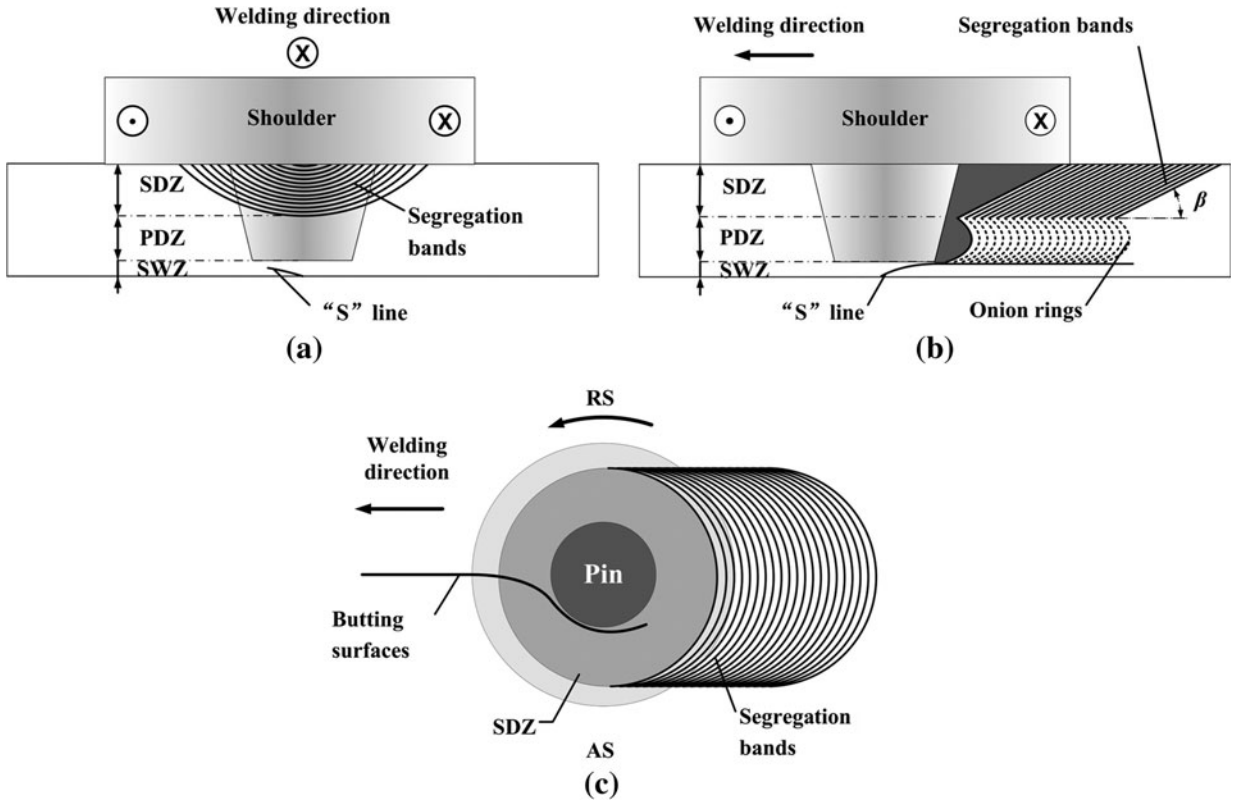

Fig. 16—Predicted patterns of segregation bands in sample H-800-100: (*a*) on the transverse cross section, (*b*) on the longitudinal cross section and (*c*) on the horizontal cross section.

was vulnerable to fracture. Thus, sample M-800-200 mostly fractured along the NZ/TMAZ interface (Figure 12(c)). Occasionally, the local strength of the NZ with the dense segregation bands may be slightly weaker than that of the NZ/TMAZ interface for sample M-800-200. Thus, the fracture of sample M-800-200 also occurred across the NZ, although the crack appeared at the RS interface of NZ/TMAZ during tension (Figure 12(b)). Original fracture along the segregation bands in the SDZ was in a transgranular fracture mode (Figure 14(c)). When the crack reached the PDZ where no continuous segregation bands existed, a tearing action occurred across the PDZ and caused the cleavage fracture under the large tensile stress (Figure 14(d)).

As the welding speed increased further from 200 to 400 mm min^{-1}, the density of segregation bands decreased (Figure 5(c)), at the same time the hardness of LHZ I increased to being higher than that of LHZ II (Figure 11). In this case, the joints fractured along either the scarce segregation bands or LHZ II in sample L-800-400 ((Figures 12(d) and (e)). The unusual fracture case (Figure 12(d)) was similar to that in sample M-800-200 (Figures 13(d), 14(e) and (f)).

The results of the current study indicated that there is a close relationship between the material flow and the distribution of secondary phases in the FSWed joints. The periodic material flow in FSW resulted in the formation of continuous segregation bands in the SDZ but produced very short segregation bands in the PDZ. This indicates that the material flow was obviously different in the SDZ and PDZ. To obtain a more complete understanding of material flow during FSW, further studies are needed, including studies of the evolution of butting surfaces and secondary phase particles, as well as their distribution in both the SDZ and the PDZ.

V. CONCLUSIONS

1. The linear segregation bands, consisting of secondary phase particles, were mainly observed in the SDZ. Their formation resulted from the periodic material flow and underwent a complicated process. Accompanied by a change in the grain structure from BM grains → elongated coarse grains (forming the long straight grain boundaries) → finer elongated grains → micron-scaled nugget grains, the secondary phase particles formed the phase aggregation bands at the high strain rate gradient region and were then partially broken and dissolved under the plastic deformation and heat input. Meanwhile, the dissolved elements migrated to the long straight grain boundaries and reprecipitated following welding, forming the segregation bands.
2. The 3D patterns of the segregation bands could be described by a set of equations. The average spacing of the segregation bands on the longitudinal and horizontal cross sections was equal to tool advancement per revolution and the tilt angle on the longitudinal cross section was consistent with the calculated value based on the shape of the SDZ on the transverse cross section.
3. The "S" line originated from the oxide film on the initial butting surfaces and experienced only the thermomechanical deformation process without a change in the chemical composition.
4. The morphologies of the segregation bands and "S" line were dependent on the welding parameters. The segregation bands were clear and dense in samples H-800-100 and M-800-200 but less distinct and scarce in sample L-800-400. However, the "S" line gradually became more and more intact as the welding speed increased from 100 to 400 mm min^{-1}.
5. When FSWed 2024Al-T351 joints were pulled along the transverse direction, the segregation bands resulted in an unusual tensile fracture behavior along the segregation bands in samples M-800-200 and L-800-400. The "S" line did not affect the tensile fracture behavior of the FSWed joints.

ACKNOWLEDGMENTS

The current study was supported by (a) the National Outstanding Young Scientist Foundation of China under Grant No. 50525103 and (b) the Hundred Talents Program of Chinese Academy of Sciences.

REFERENCES

1. F. Lefebvre, S. Ganguly, and I. Sinclair: *Mater. Sci. Eng. A*, 2005, vol. 397, pp. 338–45.
2. D. Fersini and A. Pirondi: *Eng. Fract. Mech.*, 2007, vol. 74, pp. 468–80.
3. W.M. Thomas, E.D. Nicholas, J.C. Needham, M.G. Murch, P. Templesmith, and C.J. Dawes: G.B. Patent Application No. 9125978.8, 1991.
4. M.A. Sutton, B. Yang, A.P. Reynolds, and R. Taylor: *Mater. Sci. Eng. A*, 2002, vol. 323, pp. 160–66.
5. Y.S. Sato and H. Kokawa: *Metall. Mater. Trans. A*, 2001, vol. 32A, pp. 3023–31.
6. S.R. Ren, Z.Y. Ma, and L.Q. Chen: *Scripta Mater.*, 2007, vol. 56, pp. 69–72.
7. F.C. Liu and Z.Y. Ma: *Metall. Mater. Trans. A*, 2008, vol. 39A, pp. 2378–88.
8. C.B. Fuller, M.W. Mahoney, M. Calabrese, and L. Micona: *Mater. Sci. Eng. A*, 2010, vol. 527, pp. 2233–40.
9. R. Brown, W. Tang, and A.P. Reynolds: *Mater. Sci. Eng. A*, 2009, vol. 115, pp. 513–14.
10. M.W. Mahoney, C.G. Rhodes, J.G. Flintoff, R.A. Spurling, and W.H. Bingel: *Metall. Mater. Trans. A*, 1998, vol. 29A, pp. 1955–64.
11. Y.H. Zhao, S.B. Lin, L. Wu, and F.X. Qu: *Trans. Nonferrous Met. Soc. China*, 2005, vol. 15, pp. 1248–52.
12. H.J. Liu, H. Fujii, M. Maedaa, and K. Nogi: *J. Mater. Process. Technol.*, 2003, vol. 142, pp. 692–96.
13. C. Genevois, A. Deschamps, A. Denquin, and B. Doisneau-cottignies: *Acta Mater.*, 2005, vol. 53, pp. 2447–58.
14. H. Aydin, A. Bayram, A. Uguz, and K.S. Akay: *Mater. Des.*, 2009, vol. 30, pp. 2211–2221.
15. H. Aydin, A. Bayram, A. Uguz, and I. Durgun: *Mater. Des.*, 2010, vol. 31, pp. 2568–77.
16. T.S. Srivatsan, S. Vasudevan, and L. Park: *Mater. Sci. Eng. A*, 2007, vol. 466, pp. 235–45.
17. Z. Hu, S. Yuan, X. Wang, G. Liu, and Y. Huang: *Mater. Des.*, 2011, vol. 32, pp. 5055–60.

18. K.N. Krishnan: *Mater. Sci. Eng. A*, 2002, vol. 327, pp. 246–51.
19. A.P. Reynolds: *Sci. Technol. Weld. Join.*, 2000, vol. 5, pp. 120–24.
20. Y.S. Sato, H. Takauchi, S.H.C. Park, and H. Kokawa: *Mater. Sci. Eng. A*, 2005, vol. 405, pp. 333–38.
21. N. Afrin, D.L. Chen, X. Cao, and M. Jahazi: *Mater. Sci. Eng. A*, 2005, vol. 472, pp. 179–86.
22. S. Lim, S. Kim, C.G. Lee, C.D. Yim, and S.J. Kim: *Metall. Mater. Trans. A*, 2005, vol. 36A, pp. 1609–12.
23. M. Abbasi Gharacheh, A.H. Kokabi, G.H. Daneshi, B. Shalchi, and R. Sarrafi: *Int. J. Mach. Tool. Manuf.*, 2006, vol. 46, pp. 1983–87.
24. C.Z. Zhou, X.X. Yang, and G.H. Luan: *Scripta Mater.*, 2006, vol. 54, pp. 1515–20.
25. S.S. Di, X.Q. Yang, D.P. Fang, and G.H. Luan: *Mater. Chem. Phys.*, 2007, vol. 104, pp. 244–48.
26. L. Fratini, G. Buffa, and R. Shivpuri: *Acta Mater.*, 2008, vol. 58, pp. 2056–67.
27. K. Kumar and S.V. Kailas: *Mater. Sci. Eng. A*, 2008, vol. 485, pp. 367–74.
28. Z. Zhang, B.L. Xiao, D. Wang, and Z.Y. Ma: *Metall. Mater. Trans. A*, 2011, vol. 42A, pp. 1717–26.
29. W.J. Arbegast: *Scripta Mater.*, 2008, vol. 58, pp. 372–76.
30. Z. Liu, P.H. Chong, A.N. Butt, P. Skeldon, and G.E. Thompson: *Appl. Surf. Sci.*, 2005, vol. 247, pp. 294–99.
31. D.Q. Zhu and W.J. van Ooij: *Corros. Sci.*, 2003, vol. 45, pp. 2177–97.
32. S.W. Xu and X.M. Deng: *Acta Mater.*, 2008, vol. 56, pp. 1326–41.
33. K.A.A. Hassan, P.B. Prangnell, A.F. Norman, D.A. Price, and S.W. Williams: *Sci. Tech. Weld. Joi.*, 2003, vol. 8, pp. 257–68.
34. A.P. Reynolds, W. Tang, Z. Khandkar, J.A. Khan, and K. Lindner: *Sci. Technol. Weld. Join.*, 2005, vol. 10, pp. 190–99.
35. M.W. Mahoney, C.G. Rhodes, J.G. Flintoff, R.A. Spurling, and W.H. Bingel: *Metall. Mater. Trans. A*, 1998, vol. 29A, pp. 1955–64.
36. P.A. Colegrove and H.R. Shercliff: *Sci. Technol. Weld. Join.*, 2003, vol. 8, pp. 360–68.
37. Y.S. Sato, M. Urata, and H. Kokawa: *Metall. Mater. Trans. A*, 2002, vol. 33A, pp. 625–35.
38. Z.W. Chen and S. Cui: *Scripta Mater.*, 2008, vol. 58, pp. 417–20.
39. G.R. Cui, Z.Y. Ma, and S.X. Li: *Scripta Mater.*, 2008, vol. 58, pp. 1082–85.
40. A.P. Reynolds: *Scripta Mater.*, 2008, vol. 58, pp. 338–42.
41. A. Arora, Z. Zhang, A. De, and T. DebRoy: *Scripta Mater.*, 2009, vol. 61, pp. 863–66.
42. X. Deng and S. Xu: *Trans. NAMRI/SME*, 2001, vol. 28, pp. 631–38.
43. P.B. Prangnell and C.P. Heason: *Acta Mater.*, 2005, vol. 53, pp. 3179–92.